Journal of the Ceramic Society of Japan 129 [11] 676-682 2021
DOI http://doi.org/10.2109/jcersj2.21104

JCS-Japan

FULL PAPER

Effects of noble-metal loading and ultraviolet-light irradiation on gas-sensing properties of porous indium oxide films at room temperature

Takeo HYODO[1,†], Azusa IWANAGA[2], Keijiro ISHIDA[1], Kai KAMADA[1], Taro UEDA[1] and Yasuhiro SHIMIZU[1]

[1]Graduate School of Engineering, Nagasaki University, 1–14 Bunkyo-machi, Nagasaki 852–8521, Japan
[2]School of Engineering, Nagasaki University, 1–14 Bunkyo-machi, Nagasaki 852–8521, Japan

Fundamental gas-sensing properties of porous (pr-)In_2O_3 powders loaded with and without 0.5 mass % noble metal (pr-*0.5*N/In_2O_3 and pr-In_2O_3, respectively, N: noble metal (Au or Pd)) to NO_2, H_2, and ethanol balanced with dry air were investigated at 30 °C under UV-light irradiation (main wavelength: 365 nm). The spherical pr-*0.5*N/In_2O_3 and pr-In_2O_3 powders were prepared by ultrasonic-spray pyrolysis employing polymethylmethacrylate microspheres with a diameter of ca. 70 nm, which were synthesized by ultrasonic-assisted emulsion polymerization. The Au loading largely improved the NO_2 response of the pr-In_2O_3 sensor, a ratio of the resistance in NO_2 to that in air, especially under weak UV-light irradiation, because of the relatively large resistance in air. On the other hand, the Pd loading efficiently increased the difference in the conductance of the pr-In_2O_3 sensor between in NO_2 and in air under the whole UV-light irradiation range. The UV-light irradiation is effective in improving the NO_2-sensing properties of these sensors at room temperature, but the sensing performance was a little inferior to that operated at elevated temperatures under no UV-light irradiation. These sensors also responded to reducing gases, H_2 and ethanol, under UV-light irradiation, and the responses to ethanol were much larger than those to H_2. However, the responses to both the gases were much smaller than that to NO_2.

Key-words : Semiconductor-type gas sensor, Indium oxide, Polymethylmethacrylate, Noble metal, UV-light irradiation, Nitrogen dioxide, Hydrogen, Ethanol

[Received July 5, 2021; Accepted August 23, 2021]

1. Introduction

Numerous efforts have been directed to controlling the microstructure of various ceramics to enhance their original properties as well as to add new features. Among them, the introduction of mesoporous and macroporous structures into materials have been commonly attempted by utilizing self-assembly of supramolecules[1),2)] and polymer microspheres,[3),4)] respectively, as a template. We have also developed various mesoporous and macroporous gas-sensing materials during the last two decades.[5)–15)] Among all materials, spherical oxide powders with well-developed pores, which are prepared by ultrasonic spray pyrolysis employing polymethylmethacrylate (PMMA) microsphere templates, are quite attractive as gas-sensing materials for various types of gas sensors, because they can be easily applied onto a sensor platform by conventional techniques such as screen printing. We have thus far demonstrated that semiconductor-type gas sensors fabricated with such porous oxide powders showed excellent sensing properties to various gases at elevated temperatures.[16)–20)] On the other hand, we have also developed semiconductor-type gas sensors operable at room temperature (RT) under UV-light irradiation.[21),22)] Various researchers have investigated sensing properties of semiconductor-type gas sensors assisted by UV-light irradiation to various gases,[23)–27)] and the miniaturization of these sensors by utilizing the micro-electro-mechanical system technology has also been recently attempted for the practical use.[28),29)]

In this study, porous spherical In_2O_3 (pr-In_2O_3) powders were prepared by ultrasonic spray pyrolysis employing PMMA microspheres, and the effects of noble-metal (Au or Pd) loading onto the pr-In_2O_3 powders on the gas-sensing properties at RT with and without UV-light irradiation were discussed, as compared with the gas-sensing properties at elevated temperatures.

2. Experimental

PMMA microspheres with a diameter of ca. 70 nm were synthesized by ultrasonic-assisted emulsion polymerization. The detailed procedure is described in our previous papers.[18)–20)] The PMMA-microsphere aqueous dispersion obtained (37.5 cm^3) was mixed with $In(NO_3)_3$ aqueous

† Corresponding author: T. Hyodo; E-mail: hyodo@nagasaki-u.ac.jp

solution (0.05 mol dm^{-3}, 62.5 cm^3), and an appropriate amount of $HAuCl_4$ or $Pd(NO_3)_2$ aqueous solution (0.1 mol dm^{-3}) was added to the precursor solution to load Au or Pd onto In_2O_3, respectively, in some cases. Figure S1 shows a specially designed mist-supplier for the ultrasonic spray pyrolysis. The precursor solution was poured into a plastic container with a bottom made of polystyrene film (thickness: ca. 10 μm), and then it was nebulized by an ultrasonic vibrator (Honda Electric Co., Ltd., HM-303N, 2.4 MHz). The obtained mists were fed into an electric furnace heated at 1000 °C, to prepare porous spherical In_2O_3 powders loaded with or without noble metal (pr-*n*N/In_2O_3 or pr-In_2O_3, respectively, N: noble metal (Au or Pd), *n*: the amount of N loading onto pr-In_2O_3 [mass %], *0.5* in this study). The microstructure of these powders was observed by scanning electron microscopy (SEM; JEOL Ltd., JSM-7500F). The pore-size distribution and specific surface area (SSA) of these powders were measured by Barrett–Joyner–Halenda and Brunauer–Emmett–Teller methods using N_2 adsorption/desorption isotherms (Micromeritics Inst. Corp., Tristar3000), respectively. The crystal phase of these powders was characterized by X-ray diffraction analysis (XRD; Rigaku Corp., RINT2200) using Cu Kα radiation, and their crystallite size (CS) was calculated from the (222) diffraction peak using the Scherrer equation.

The pr-In_2O_3 or pr-*0.5*N/In_2O_3 powder was mixed with an appropriate amount of α-terpineol, and the paste obtained was screen printed onto an alumina substrate equipped with a pair of interdigitated Pt electrodes (gap size: ca. 200 μm). After drying at 100 °C, they were heat-treated at 550 °C for 5 h in ambient air. The responses of these sensors to 1–20 ppm NO_2, 6,000 ppm H_2, and 50 ppm ethanol balanced with dry air were measured at 30 °C at a flow rate of 100 cm^3 min^{-1} under UV-light irradiation using a light-emitting diode (UV-LED, ARK TECH Co., Ltd., LS-4A1-1, main wavelength: 365 nm), after pre-heat treatment at 200 °C for several tens of minutes in dry air. The volume containing the gas-flow pathway and the rectangular container (*V*), in which the sensors are set, is ca. 106 cm^3.[22] In addition, the response of these sensors to 5 ppm NO_2 balanced with dry air at elevated temperatures (200–500 °C) was also measured at a flow rate of 100 cm^3 min^{-1} under no UV-light irradiation. The cylindrical container used (*V*: ca. 106 cm^3) was heated in an electric furnace.[16)–18)]

3. Results and discussion

Figure S2 shows XRD spectra of all the powders. All the peaks of these powders were assigned to cubic In_2O_3 (JCPDF No. 6-416), and no peaks derived from Au and Pd were in the spectra of the pr-*0.5*Au/In_2O_3 and pr-*0.5*Pd/In_2O_3 powders, respectively, because of the small amount and/or small size of Au and Pd nanoparticles loaded onto the In_2O_3 powders. In addition, the loading of Au or Pd onto In_2O_3 had little influence on their CSs, but the CSs of the pr-*0.5*Au/In_2O_3 and pr-*0.5*Pd/In_2O_3 powders (ca. 14.2 nm and ca. 14.3 nm, respectively) were slightly smaller than that of pr-In_2O_3, (ca. 14.5 nm). Figure S3 shows nitrogen adsorption/desorption isotherms and pore-size distributions of these powders, together with their SSAs. All the powders had well-developed porous structures with centered diameters of ca. 67–81 nm and ca. 30 nm, which were calculated from nitrogen adsorption and desorption isotherms, respectively, because they had a hysteresis loop in the nitrogen adsorption/desorption isotherms in the relatively high-pressure range. These results indicate that their well-developed porous structure mainly consists of well-developed ink-bottle pores with narrow necks (ca. 30 nm) and wide bodies (ca. 67–81 nm). In addition, these powders had a large number of mesopores with a diameter of less than 10 nm, and the pore-size distribution and the pore volume were largely dependent on the amounts and the kinds of N loaded onto pr-In_2O_3. Namely, the Au loading mainly decreased the amounts of pores with a diameter of ca. 2–10 nm, while the Pd loading increased the amounts of pores with a diameter of less than 2 nm. They are the reasons why the Au and Pd loading decreased and increased SSA of the pr-In_2O_3 powder, respectively. Figure S4 shows SEM photographs of the pr-In_2O_3 and pr-*0.5*Au/In_2O_3 powders. The morphology of these powders obtained was spherical, and a large number of circular pores were confirmed on the surface. The size of these circular pores was almost correspondent to the centered diameter, ca. 30 nm which was estimated from their N_2 desorption isotherms.

Figure 1 shows cross-sectional SEM photographs of all the sensors. The oxide-film thicknesses of the pr-In_2O_3, pr-*0.5*Au/In_2O_3, and pr-*0.5*Pd/In_2O_3 sensors were ca. 15 μm, ca. 20 μm, and ca. 17 μm, respectively, and there was little difference in the stacking state of their spherical particles among these sensors. This fact indicates that the loading of Au or Pd onto In_2O_3 has little impact on the microstructure of the films and thus that the gas-sensing properties of these sensors can be clearly evaluated without respect to the geometric characteristics of the oxide films. **Figure 2** shows response transients of all the sensors to 5 ppm NO_2 at 30 °C in dry air under UV-light irradiation of 0–129 mW cm^{-2}, and the variations in the magnitude of their NO_2 responses with UV-light intensity were summarized in **Fig. 3**. Here, the NO_2 response (R_g/R_a) was defined as a ratio of the resistance in NO_2 balanced with dry air (R_g) to that in dry air (R_a). The loading of Au or Pd onto In_2O_3 reduced the resistance of the pr-In_2O_3 sensor in dry air under no UV-light irradiation. Figure S5 shows energy-band diagrams of interfaces between loaded materials (PdO, Pd, and Au) and In_2O_3. Generally, the work function (φ) of Au (ca. 5.1 eV)[30)] and Pd (4.8 eV)[31)] [or PdO (ca. 5.5 eV)[31)]] bulks is larger than that of In_2O_3 bulk (ca. 4.3 eV).[32)] On the basis of these values, the resistance of the pr-*0.5*Au/In_2O_3 and pr-*0.5*Pd/In_2O_3 sensors should be larger than that of the pr-In_2O_3 sensor. Actually, the resistance of In_2O_3 loaded with Au by general impregnation was larger than that of pristine In_2O_3.[33)–35)] However, Zhang et al. clarified that the work function of Au nanoparticles monotonically decreased with a decrease in the particle size by Kelvin probe force microscopy and that the

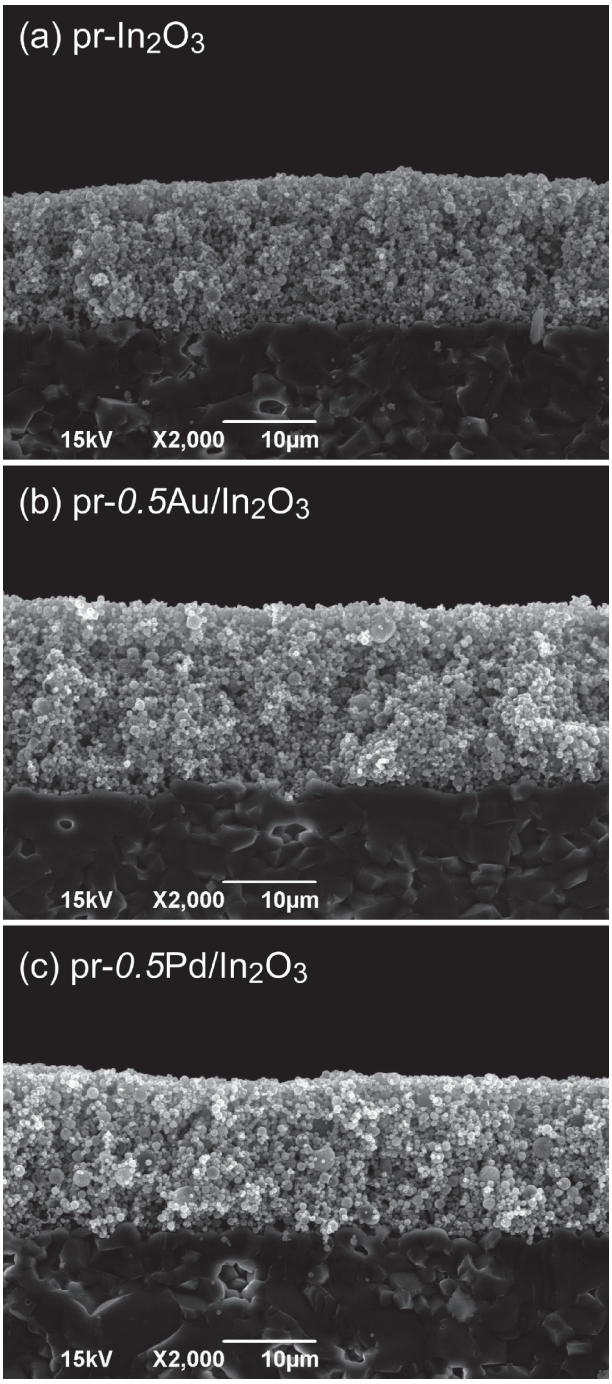

Fig. 1. Cross-sectional SEM photographs of all sensors.

work function of a Au nanoparticle with a diameter of 10 nm reached only ~3.6 eV.[30] In this case, electrons transfer from the Au nanoparticle to In_2O_3, and thus the energy-band diagram of the interface is shown in Fig. S5(c)(ii). This is considered to be the reason why the resistance of the pr-*0.5*Au/In_2O_3 sensor was lower than that of the pr-In_2O_3 sensor. It is expected that Au components are highly dispersed in the pr-*0.5*Au/In_2O_3 powder, because it is prepared by instantaneous heating of aqueous precursor mists containing $HAuCl_4$ as well as $In(NO_3)_3$. Actually, Au nanoparticles cannot be observed even by transmission electron microscope.[36] In addition, the resistance of the pr-*n*Au/In_2O_3 decreased with an increase in *n* in the range of 0–1.5 mass %.[36] This behavior indicates that the number of Au nanoparticles with work function smaller than that of pr-In_2O_3 increased with an increase in *n*. On the other hand, the resistance of the pr-*n*Au/In_2O_3 increased with an increase in *n* in the range of more than 1.5 mass %,[36] because the number of large Au nanoparticles with work function larger than that of pr-In_2O_3 increased with an increase in *n*. We do not have findings on the size dependence on the work function concerning Pd and PdO nanoparticles, but the loading of Pd and/or PdO by general impregnation technique also increased the resistance of various oxide films.[22),34] Therefore, it is expected that the work function of Pd and/or PdO nanoparticles would decrease with a decrease in size.[20]

The weak UV-light irradiation of 0.57 mW cm^{-2} decreased the resistance of the pr-In_2O_3 and pr-*0.5*Pd/In_2O_3 sensors in dry air, since electrons were excited from the valence band to the conduction band to increase the carrier density. By contrast, the weak UV-light irradiation increased the resistance of the pr-*0.5*Au/In_2O_3 in dry air. This is probably because the number of oxygen adsorbates increased on the Au surface and/or at the boundary between Au and In_2O_3 through the activated adsorption by the weak UV-light irradiation [Eq. (1)], and the number of electrons trapped by the oxygen adsorbates was larger than the number of electrons produced by the UV-light irradiation.

$$O_2 + e^- \rightarrow O_2^- \quad (1)$$

Degler et al. also suggested that the number of negatively charged oxygen adsorbates was increased by the loading of Au onto SnO_2 surface.[37] Most Pd nanoparticles loaded on pr-In_2O_3 are originally oxidized to form PdO,[20),22] and thus the number of oxygen adsorbates which is increased by the weak UV-light irradiation is much smaller than that of electrons excited. This is likely to be the reason why the weak UV-light irradiation decreased the resistance of the pr-*0.5*Pd/In_2O_3 sensor. Further increase in the intensity of the UV-light irradiation monotonically decreased the resistance of all the sensors.

The introduction of NO_2 into dry air increased the resistance of all the sensors, both with and without UV irradiation, because the adsorption of NO_2 molecules on the surface decreased the concentration of free electrons in the oxide films [Eq. (2)] and its effect was much larger than that of oxygen adsorbates.

$$NO_2 + e^- \rightarrow NO_2^- \quad (2)$$

These sensors all showed the largest responses to 5 ppm NO_2 under no UV-light irradiation. However, their response and recovery speeds under no UV-light irradiation were much slower than those under UV-light irradiation. The adsorption of NO_2 is commonly dominant over that of O_2 on the oxide surface from the viewpoint of equilibrium. Besides, NO_2 molecules form deeper acceptor levels on the oxide surface than the negatively charged oxygen adsorbates (O_2^-).[38] They are the main reasons of

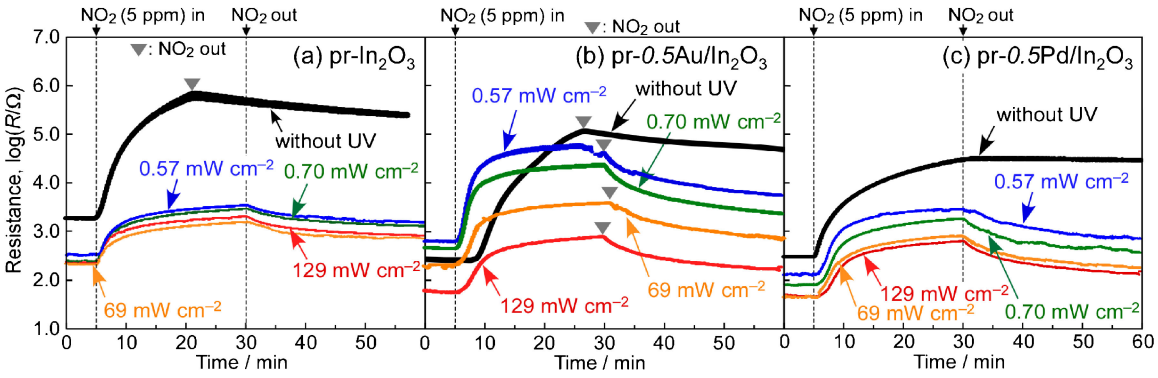

Fig. 2. Response transients of all sensors to 5 ppm NO_2 at 30 °C in dry air under UV-light irradiation of 0–129 mW cm^{-2}.

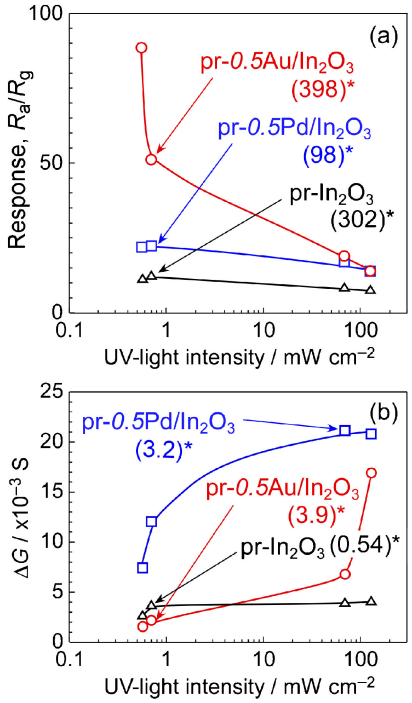

Fig. 3. Variations in (a) responses and (b) ΔG of all sensors to 5 ppm NO_2 at 30 °C in dry air with UV-light intensity. *Values under no UV-light irradiation in parentheses.

the large resistance of the sensors in NO_2 balanced with air. However, the behavior of these sensors indicates that the rates of adsorption and desorption of NO_2 molecules onto and from the oxide surface are quite slow from the viewpoint of kinetics, because of the shortage of driving energy at 30 °C. The weak UV-light irradiation even accelerated the response and recovery speeds of all the sensors, whereas it decreased the responses of all sensors. Among them, the pr-*0.5*Au/In_2O_3 sensor showed the largest NO_2 response under the smallest UV-light irradiation (0.57 mW cm^{-2}) and its response to 5 ppm NO_2 obviously decreased with an increase in the intensity of UV-light irradiation. On the other hand, the responses of pr-In_2O_3 and pr-*0.5*Pd/In_2O_3 sensors were drastically decreased even by the small UV-light irradiation and they tended to decrease gradually with an increase in the intensity of UV-light irradiation, as shown in Fig. 3(a). The response and recovery speeds of all the sensors were hardly dependent on the intensity of UV-light irradiation. Figure 3(b) shows the dependences of the difference in conductance between in air and in NO_2 (ΔG) on the intensity of UV-light irradiation. It has been confirmed that the temperature of all the sensors was 30 °C under operation with and without UV-light irradiation. Given that the electron mobility (μ) was not dependent on the UV-light intensity at all, therefore, ΔG is proportional to the difference in carrier (electron) concentration between in air and in NO_2 (Δn_e ($n_{e,a}$–$n_{e,g}$), $n_{e,a}$ and $n_{e,g}$: carrier concentration in dry air and in target gas, respectively), as shown in the following equation,

$$\Delta G = \frac{1}{R_a} - \frac{1}{R_g} = Ae\mu\Delta n_e \quad (3)$$

where e and A stand for elementary charge and geometric coefficient, respectively. Even the smallest UV-light irradiation of 0.57 mW cm^{-2} increased Δn_e of the pr-In_2O_3 and pr-*0.5*Pd/In_2O_3 sensors, which indicates the increase in the number of NO_2 adsorbates on the surface. However, the responses of the pr-In_2O_3 and pr-*0.5*Pd/In_2O_3 sensors decreased even though the number of NO_2 adsorbates was increased by the UV-light irradiation. This tendency originates from a decrease in the resistance (an increase in $n_{e,a}$) in air. On the other hand, $n_{e,a}$ of the pr-*0.5*Au/In_2O_3 sensor was decreased by the smallest UV-light irradiation of 0.57 mW cm^{-2}, and thus it was smaller than those of the pr-In_2O_3 and pr-*0.5*Pd/In_2O_3 sensors. Nevertheless, the response of the pr-*0.5*Au/In_2O_3 sensor was much larger than those of the pr-In_2O_3 and pr-*0.5*Pd/In_2O_3 sensors. That is because $n_{e,a}$ of the pr-*0.5*Au/In_2O_3 sensor in air, which is much smaller than those of the pr-In_2O_3 and pr-*0.5*Pd/In_2O_3 sensors, increased the relative ratio of $n_{e,g}$ to $n_{e,a}$ ($n_{e,g}/n_{e,a}$). Furthermore, Δn_e of all the sensors increased with an increase in the UV-light intensity to a greater or lesser, and thus their responses decreased with an increase in the intensity of the UV-light irradiation.

Figure 4 shows response transients of the pr-*0.5*Au/In_2O_3 sensor to 1–20 ppm NO_2 at 30 °C in dry air and the NO_2-concentration dependence on the magnitude of the NO_2 response, under the UV-light irradiation of 0.7 mW cm^{-2}. The NO_2 response simply increased with an

increase in concentration. The response to less than 1 ppm NO_2 was not measured in this study, but it should abruptly rise in the range of sub-ppm concentration of NO_2, as shown by the dashed line. On the other hand, the responses to higher concentrations of NO_2 ($\geq$15 ppm) increased without attaining saturation. The relationship between the response and the concentration is similar to those of the N_2 adsorption/desorption isotherms at −196 °C under the low relative pressure region of 0–0.5 (see Fig. S3). As mentioned below, the interaction between negatively adsorbed NO_2 molecules and the oxide surface is quite large. In addition, it is also well-known that various types of nitrogen oxides such as nitrate species (NO_3^-) are on the oxide surface.[39)–41)] The interaction among these NOx-based adsorbates as well as between the NOx-based adsorbates and the oxide surface under UV-light irradiation may promote the number and/or the adsorption strength of their NOx-based adsorbates. Moreover, a certain amount of NO_2 molecules was easily converted to NO and atomic oxygen under UV-light irradiation and they reacted one another, as shown below.[42)]

$$NO_2 + h\nu \rightarrow NO + O \quad (4)$$

$$O + O_2 \rightarrow O_3 \quad (5)$$

$$NO + O_3 \rightarrow NO_2 + O_2 \quad (6)$$

These reactions must also complicatedly influence the concentration dependence on the NO_2 response. Hereafter, we should spectroscopically investigate these phenomena in detail.

The effects of operating temperatures (200–500 °C) on the NO_2 response of all the sensors were compared with those of UV-light irradiation. **Figure 5** shows response transients of pr-In_2O_3, pr-*0.5*Au/In_2O_3, and pr-*0.5*Pd/In_2O_3 sensors to 5 ppm NO_2 at elevated temperatures in dry air under no UV-light irradiation. The resistance of the pr-In_2O_3 sensor monotonically decreased with an increase in temperature, whereas that of the pr-*0.5*Pd/In_2O_3 sensor was hardly dependent on temperature. The variation in resistance of the pr-*0.5*Au/In_2O_3 sensor with temperature was quite complicated. Namely, the resistance of the pr-*0.5*Au/In_2O_3 sensor decreased with an increase in temperature at least to 200 °C, but it increased with an increase in temperature between 200 and 400 °C. This dependence of the resistance in air on the operating temperature under no UV-light irradiation is different from that on the intensity of the UV-light irradiation at 30 °C, probably because the rise in operating temperature increased the number of oxygen adsorbates on the pr-In_2O_3 surface by the spillover effect from Au nanoparticles loaded[37)] and changed the species of oxygen adsorbates from O_2^- to O^- and O^{2-} in the temperature range. In addition, the Au loading onto the pr-In_2O_3 surface was slightly effective in enhancing the NO_2 response only at 200 °C. The responses of all the sensors at elevated temperatures under no UV-light irradiation were relatively larger than those at 30 °C under UV-light irradiation. The largest NO_2 responses of all the sensors were attained at 200 °C and they decreased with an increase in temperature. This tendency is similar to the

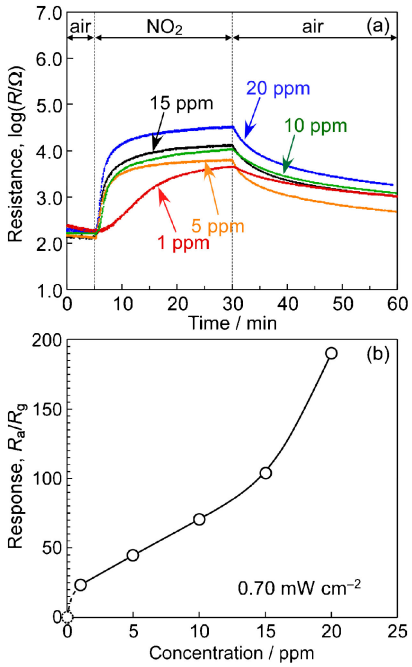

Fig. 4. (a) Response transients of pr-*0.5*Au/In_2O_3 sensor to 1–20 ppm NO_2 at 30 °C in dry air and (b) NO_2-concentration dependence on NO_2 response, under UV-light irradiation of 0.7 mW cm^{-2}.

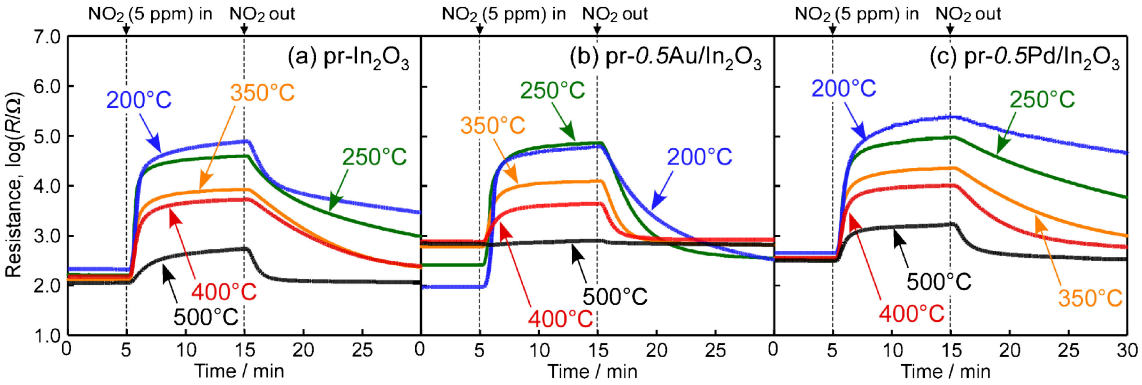

Fig. 5. Response transients of all sensors to 5 ppm NO_2 at elevated temperatures in dry air under no UV-light irradiation.

behavior under UV-light irradiation, which indicates that further reduction in the intensity of the UV-light irradiation enhanced the NO_2 responses of these sensors. On the other hand, the difference in response and recovery speeds between at 30 °C under UV-light irradiation and at elevated temperatures under no UV-light irradiation cannot be discussed because the shape of the test chambers and their dead volume were different between these measurement conditions.

Figure S6 shows response transients of pr-In_2O_3, *0.5*Au/pr-In_2O_3, and *0.5*Pd/pr-In_2O_3 sensors to 6,000 ppm H_2 and 50 ppm ethanol at 30 °C in dry air under UV-light irradiation, and the variations in the magnitude of their responses to 6,000 ppm H_2 and 50 ppm ethanol with the intensity of UV-light irradiation were summarized in Fig. S7(a). Here, the responses to these reducing gases (R_a/R_g) were defined as a ratio of the resistance in dry air (R_a) to that in H_2 or ethanol balanced with dry air (R_g). The pr-In_2O_3 sensor showed a slight response to 6,000 ppm H_2, which decreased with an increase in the intensity of UV-light irradiation. In addition, the response and recovery speeds of the pr-In_2O_3 sensor were quite slow under every UV-light irradiation. On the other hand, the response of the pr-In_2O_3 sensor to 50 ppm ethanol was larger than that to 6,000 ppm H_2, and the magnitude of its ethanol response increased and its response and recovery speeds gradually accelerated with an increase in the intensity of UV-light irradiation. The N loading increased the H_2 response of the pr-In_2O_3 sensor, especially under small UV-light irradiation, while it was not so effective in improving the response and recovery speeds. On the other hand, the Pd loading enhanced the ethanol response especially under large UV-light irradiation, while the Au loading was ineffective in improving the ethanol response. Figure S7(b) shows the dependences of the difference in conductance between in target gases (6000 ppm H_2 or 50 ppm ethanol) and in air (ΔG) on the intensity of UV-light irradiation. Considering ΔG of all the sensors to 6000 ppm H_2 are relatively small and not dependent on the intensity of UV-light irradiation, the oxidation of H_2 with oxygen adsorbates on the surface does not proceed efficiently under UV-light irradiation even by the N loading, and thus the H_2 responses of all the sensors were smaller than we expected. As ΔG of all the sensors to 50 ppm ethanol simply increased with an increase in the intensity of UV-light irradiation, the UV-light irradiation was effective in enhancing the oxidation of ethanol with oxygen adsorbates on the surface. The Pd loading is the most effective way to enhance the oxidation of ethanol as well as to improve the ethanol response on the pr-In_2O_3 surface.

4. Conclusion

Sensing properties of pr-In_2O_3 and pr-*0.5*N/In_2O_3 sensors (N: Au or Pd) to NO_2, H_2, and ethanol balanced with dry air were investigated at 30 °C under UV-light irradiation (main wavelength: 365 nm). The weak UV-light irradiation increased the resistance of the pr-*0.5*Au/In_2O_3 sensor in dry air, probably because of an increase in the number of oxygen adsorbates. Thus, the NO_2 response of the pr-*0.5*Au/In_2O_3 sensor was much larger than that of the pr-In_2O_3 sensor under weak UV-light irradiation. On the other hand, the pr-*0.5*Pd/In_2O_3 sensor showed the largest ΔG to NO_2 under every UV-light irradiation range. This indicates that the amount of NO_2 adsorbed on the surface of the pr-*0.5*Pd/In_2O_3 sensor was much larger than that of other sensors. The operation of these sensors at elevated temperatures especially at 200–250 °C was effective in improving the NO_2-sensing properties of these sensors under no UV-light irradiation, in comparison with the mild operation at 30 °C under UV-light irradiation. Hereafter, the optimization of the operating condition as well as the compositional and microstructural controls of the pr-*n*N/In_2O_3 sensor are essential in improving their NO_2-sensing properties at RT under UV-light irradiation. In addition, these sensors also responded to 6,000 ppm H_2 and 50 ppm ethanol at 30 °C in dry air under UV-light irradiation. Especially, the strong UV-light irradiation to pr-*0.5*Pd/In_2O_3 sensor efficiently enhanced the ethanol response.

References

1) T. Yanagisawa, T. Shimizu, K. Kuroda and C. Kato, *B. Chem. Soc. Jpn.*, 63, 988–992 (1990).
2) J. S. Beck, J. C. Vartuli, W. J. Roth, M. E. Leonawicz, C. T. Kreage, K. D. Schmitt, D. T.-W. Chu, D. H. Olson, E. W. Sheppard, S. B. McCullen, J. B. Higgins and J. L. Schlenker, *J. Am. Chem. Soc.*, 114, 10834–10854 (1992).
3) A. Imhof and D. J. Pine, *Nature*, 389, 948–951 (1997).
4) B. T. Holland, C. F. Blanford and A. Stein, *Science*, 281, 538–540 (1998).
5) T. Hyodo, N. Nishida, Y. Shimizu and M. Egashira, *J. Ceram. Soc. Jpn.*, 109, 481–483 (2001).
6) T. Hyodo, N. Nishida, Y. Shimizu and M. Egashira, *Sensor. Actuat. B-Chem.*, 83, 209–215 (2002).
7) T. Hyodo, S. Abe, Y. Shimizu and M. Egashira, *Sensor. Actuat. B-Chem.*, 93, 590–600 (2003).
8) M. Hayashi, T. Hyodo, Y. Shimizu and M. Egashira, *Sensor. Actuat. B-Chem.*, 141, 465–470 (2009).
9) Y. Yuzuriha, T. Hyodo, T. Sasahara, Y. Shimizu and M. Egashira, *Sens. Lett.*, 9, 409–413 (2011).
10) K. Sasahara, T. Hyodo, Y. Shimizu and M. Egashira, *J. Eur. Ceram. Soc.*, 24, 1961–1967 (2004).
11) T. Hyodo, K. Sasahara, Y. Shimizu and M. Egashira, *Sensor. Actuat. B-Chem.*, 106, 580–590 (2005).
12) H. Seh, T. Hyodo and H. L. Tuller, *Sensor. Actuat. B-Chem.*, 108, 547–552 (2005).
13) I.-D. Kim, A. Rothschild, T. Hyodo and H. L. Tuller, *Nano Lett.*, 6, 193–198 (2006).
14) M. Morio, T. Hyodo, Y. Shimizu and M. Egashira, *Sensor. Actuat. B-Chem.*, 139, 563–569 (2009).
15) T. Hyodo, Y. Takakura, K. Kuroiwa, K. Tsuchiya and Y. Shimizu, *J. Nanosci. Nanotechno.*, 19, 5351–5360 (2019).
16) K. Hieda, T. Hyodo, Y. Shimizu and M. Egashira, *Sensor. Actuat. B-Chem.*, 133, 144–150 (2008).
17) T. Hyodo, H. Inoue, H. Motomura, K. Matsuo, T. Hashishin, J. Tamaki, Y. Shimizu and M. Egashira, *Sensor. Actuat. B-Chem.*, 151, 265–273 (2010).
18) T. Hyodo, E. Fujii, K. Ishida, T. Ueda, Y. Shimizu and

M. Egashira, *Sensor. Actuat. B-Chem.*, **244**, 992–1003 (2017).
19) T. Ueda, I. Boehme, T. Hyodo, Y. Shimizu, U. Weimar and N. Barsan, *Chemosensors*, **8**, 72 (2020).
20) N. Tammanoon, T. Iwamoto, T. Ueda, T. Hyodo, A. Wisitsoraat, C. Liewhiran and Y. Shimizu, *ACS Appl. Mater. Inter.*, **12**, 41728–41739 (2020).
21) F. H. Saboor, T. Ueda, K. Kamada, T. Hyodo, Y. Mortazavi, A. Ali Khodadadi and Y. Shimizu, *Sensor. Actuat. B-Chem.*, **223**, 429–439 (2016).
22) T. Hyodo, K. Urata, K. Kamada, T. Ueda and Y. Shimizu, *Sensor. Actuat. B-Chem.*, **253**, 630–640 (2017).
23) E. Comini, A. Cristalli, G. Faglia and G. Sberveglieri, *Sensor. Actuat. B-Chem.*, **65**, 260–263 (2000).
24) T. Wagner, J. Hemmemann, C.-D. Kohl and M. Tiemann, *Thin Solid Films*, **520**, 918–921 (2011).
25) H. Jin and H. Haick, *Sensor. Actuat. B-Chem.*, **237**, 30–40 (2016).
26) F. Xu and H.-P. Ho, *Micromachines-Basel*, **8**, 333 (2017).
27) A. Chizkov, M. Rumyantseva and A. Gaskov, *Nanomaterial*, **11**, 892 (2021).
28) I. Cho, Y. C. Sim, M. Cho, Y.-H. Cho and I. Park, *ACS Sensors*, **5**, 563–570 (2020).
29) M. T. Vijjapu, S. G. Surya, S. Yuvaraja, X. Zhang, H. N. Alshareef and K. N. Salama, *ACS Sensors*, **5**, 984–993 (2020).
30) Y. Zhang, O. Pluchery, L. Caillard, A.-F. Lamic-Humblot, S. Casale, Y. J. Chabal and M. Salmeron, *Nano Lett.*, **15**, 51–55 (2015).
31) S. Matsushima, T. Maekawa, J. Tamaki, N. Miura and N. Yamazoe, *J. Chem. Soc. Jpn.*, **12**, 1677–1683 (1991).
32) O. Lang, C. Pettenkofer, J. F. Sánchez-Royo, A. Segura, A. Klein and W. Jaegermann, *J. Appl. Phys.*, **86**, 5687–5691 (1999).
33) Y. Takao, M. Nakanishi, T. Kawaguchi, Y. Shimizu and M. Egashira, *Sensor. Actuat. B-Chem.*, **24–25**, 375–379 (1995).
34) M. Egashira, Y. Shimizu, Y. Takao and Y. Fukuyama, *Sensor. Actuat. B-Chem.*, **33**, 89–95 (1996).
35) T. Hyodo, Y. Tominaga, T. Yamaguchi, A. Kawahara, H. Katsuki, Y. Shimizu and M. Egashira, *Electrochemistry*, **71**, 481–484 (2003).
36) T. Ueda, K. Ishida, K. Kamada, T. Hyodo and Y. Shimizu, *Front. Mater.*, **6**, 81 (2019).
37) D. Degler, S. Rank, S. Müller, H. W. Pereira de Carvalho, J.-D. Grunwaldt, U. Weimar and N. Barsan, *ACS Sensors*, **1**, 1322–1329 (2016).
38) B. Ruhland, T. Becker and G. Müller, *Sensor. Actuat. B-Chem.*, **50**, 85–94 (1998).
39) J. Baltrusaitis, P. M. Jayaweera and V. H. Grassian, *Phys. Chem. Chem. Phys.*, **11**, 8295–8305 (2009).
40) F. Zasada, P. V. B. Pinho, W. Piskorz, C. Hudy, J. Janas, J. Gryboś, K. Góra-Marek and Z. Sojka, *J. Phys. Chem. C*, **124**, 19681–19697 (2020).
41) X. Han, H. G. W. Godfrey, L. Briggs, A. J. Davies, Y. Cheng, L. L. Daemen, A. M. Sheveleva, F. Tuna, E. J. L. Mclnnes, J. Sun, C. Drathen, M. W. George, A. J. Ramirez-Cuesta, K. M. Thomas, S. Yang and M. Schröder, *Nat. Mater.*, **17**, 691–696 (2018).
42) K. L. Kenty, N. D. Poor, K. G. Kronmiller, W. McClenny, C. King, T. Atkeson and S. W. Cambell, *Atmos. Environ.*, **41**, 4270–4280 (2007).